

Large spontaneous Hall effect in magnetic Weyl semimetallic $\text{Sm}_2\text{Ir}_2\text{O}_7$ (111) epitaxial thin films

Mithun Ghosh  and P. S. Anil Kumar *Department of Physics, Indian Institute of Science, Bangalore 560012, Karnataka, India*

(Received 25 March 2023; revised 3 July 2023; accepted 1 August 2023; published 21 August 2023)

Here, we present magnetotransport properties of $\text{Sm}_2\text{Ir}_2\text{O}_7$ (111) single-crystalline epitaxial thin films grown with different strengths of compressive strain. A long-range magnetic ordering of Ir^{4+} moments is confirmed around the observed metal-semimetal transition. The low-temperature (2–20 K) resistivity data signify a gapless semimetallic charge transport. The high-temperature (above the transition) metallic part shows a non-Fermi-liquid behavior with a resistivity saturation, highlighting the importance of electron correlation in the $5d$ electron system. Magnetoresistance (MR) measurements for the applying field along the [111] direction suggest that at low temperatures (below 10 K), the all-in-all-out/all-out-all-in (AIAO/AOAI) spin structure is stable enough against the applied magnetic field. However, from 10 K onward, observation of a hysteretic MR implies that applying a magnetic field causes a change in the spin structure (from AIAO to three-out-one-in) and a plastic domain deformation. The Hall resistivity data show an anomalous/spontaneous Hall effect in the AIAO/AOAI antiferromagnetic phase. We have found that an epitaxial strain changes the sign as well as the magnitude of the anomalous Hall component, possibly by the modification of the electronic band dispersion and associated Berry curvature [$\Omega(\vec{k})$]. Observation of an epitaxial strain-induced large spontaneous Hall effect ($\sim 50 \mu\Omega \text{ cm}$, at 7 K) identifies the presence of Weyl points and the Weyl semimetallic phase of $\text{Sm}_2\text{Ir}_2\text{O}_7$. It highlights the role of epitaxial strain in discovering new topological phases. These findings deepen our understanding of the anomalous Hall effect in $\text{Sm}_2\text{Ir}_2\text{O}_7$ and provide a practical tuning knob to manipulate the Berry curvature and related topological properties in a wide range of quantum materials.

DOI: [10.1103/PhysRevB.108.075145](https://doi.org/10.1103/PhysRevB.108.075145)

I. INTRODUCTION

Correlated $5d$ electron systems, especially transition metal oxides (TMOs) such as iridates, have received considerable attention due to the presence of spin-orbit coupling (λ) and on-site Coulomb interactions (U) of comparable strength, resulting in many novel topological electronic phases like Weyl semimetal (WSMs) and correlated topological insulators [1–5]. Crystallization of TMOs occurs in a wide variety of structures. Among those the pyrochlore iridate ($RE_2\text{Ir}_2\text{O}_7$) family attained considerable interest, which shows thermally driven [6] as well as chemically tuned [7,8] (by varying ionic radii of RE^{3+}) metal-insulator transitions occurring concomitantly with the onset of magnetic ordering, and the electronic ground state is predicted to be a magnetic WSM [2]. Many other nontrivial transports and topological properties, such as non-Fermi-liquid (NFL) behavior [9], giant magnetoresistance [10], magnetic-field-induced quantum phase transitions [11,12], and anomalous, spontaneous, and topological Hall effects [13,14], have been experimentally observed in many pyrochlore iridate compounds. Out of all the pyrochlore iridates, our focus is on $\text{Sm}_2\text{Ir}_2\text{O}_7$ because its sister compounds like (Eu, Nd, Pr) $_2\text{Ir}_2\text{O}_7$ having a very close lattice parameter already show experimental signatures of WSMs [14–17]. In addition, in the paramagnetic metallic phase of $\text{Pr}_2\text{Ir}_2\text{O}_7$ the electronic band structure shows a quadratic band touching at the Fermi level (E_F) [18], and by small time-reversal symmetry breaking perturbations the Fermi node can also lead to Weyl points (WPs) close to the E_F .

Bulk (single or polycrystal) $\text{Sm}_2\text{Ir}_2\text{O}_7$ shows a thermally driven transition from paramagnetic metallic to antiferromagnetic (AFM) insulating state around 117 K [7]. This AFM ordering which breaks spontaneous time-reversal symmetry is a prerequisite to realize the magnetic WSM phase. In the pyrochlore lattice, both the Sm^{3+} and Ir^{4+} cation sublattice arrange in an alternating triangular and kagome geometry, which will look like corner-sharing tetrahedra along the [111] direction. The Sm^{3+} and Ir^{4+} sublattices are displaced from each other by $1/4$ of the cubic body diagonal along the [111] direction [as shown in Fig. 1(a)]. In this corner-sharing tetrahedral lattice geometry, due to Ising anisotropy in the ground state ($H = 0$), the Ir^{4+} magnetic moments order in a highly geometrical frustrated all-in-all-out/all-out-all-in (AIAO/AOAI) antiferromagnetic spin structure [shown in Fig. 1(b)]. Each of the Ir^{4+} moments (red spheres) will be surrounded by a hexagonal ring of Sm^{3+} (blue spheres), the arrangement of which in the [111] plane is shown in Fig. 1(b). This AIAO/AOAI ground state magnetic structure of Ir^{4+} $5d$ moments is confirmed by earlier muon-spin relaxation and x-ray magnetic circular dichroism studies [19,20]. This complex frustrated magnetic structure opens up new opportunities for studying the field-induced modification of the spin structure by tuning the strength of different magnetic interactions and exploring the associated electronic and magnetic properties, which remain entirely unexplored for $\text{Sm}_2\text{Ir}_2\text{O}_7$.

Besides the complex spin structure, the electronic band structure calculation based on the local density approximation

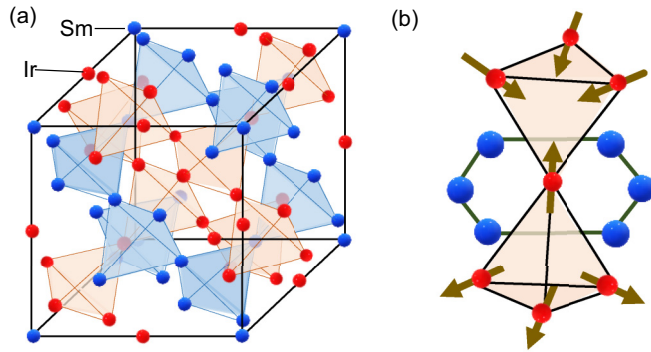


FIG. 1. (a) A unit cell of $\text{Sm}_2\text{Ir}_2\text{O}_7$ with only the cation sublattices is shown. For clarity, oxygen atoms are not shown. (b) All-in-all-out/all-out-all-in magnetic structure of Ir^{4+} $5d$ moments in corner-sharing Ir tetrahedra surrounded by a Sm^{3+} hexagonal ring in the (111) plane.

(LDA)+ U shows a 3D semimetal phase associated with the AIAO/AOAI antiferromagnetic order. In addition to the linear nondegenerate band crossing in the bulk of the Brillouin zone (BZ), the existence was predicted of the topologically protected chiral Fermi arc on the surface of the BZ, which can be detected by direct spectroscopy like angle-resolved photoemission spectroscopy experiments [2]. However, it is unclear whether this noncleavable 3D material is experimentally friendly in the surface-sensitive probe. Consequently, theoretical calculations for the WSM phase of pyrochlore iridates predicted observation of large anomalous Hall conductivity (AHC) in its thin film geometry [3,21]. So, observation of the AHC (σ_{xy}^{AHC}) will interestingly reflect the position of the WPs inside the BZ and a magnetotransport signature of the WSM phase. Due to the extreme difficulties in fabricating high-quality epitaxial thin films, until now, all the experimental studies on $\text{Sm}_2\text{Ir}_2\text{O}_7$ have been done on bulk samples only. In addition, in the thin film geometry, the growth orientation can be nicely controlled and offers lattice deformations by introducing epitaxial strain in the films. One of the aims of this study is to realize the bulk signature (observation of AHC) of the predicted WSM phase in $\text{Sm}_2\text{Ir}_2\text{O}_7$ (111) thin films by modulating the electronic band structure and the associated Berry curvature [$\Omega(\vec{k})$] with the introduction of finite epitaxial strain in the films.

In this paper, we have performed a magnetization and magnetotransport study on $\text{Sm}_2\text{Ir}_2\text{O}_7$ (111) epitaxial thin films to realize the theoretically predicted magnetic WSM phase. The longitudinal resistivity data exhibit a metal-semimetal transition around 100 K, very close to its bulk counterpart. The low-temperature (below 10 K) magnetoresistance (MR) shows spin-canting nonhysteretic negative MR. On the other hand, MR data for the temperature range of 10–100 K show finite hysteresis, which is a manifestation of the field-induced modification of Ir^{4+} spin structure and plastic domain deformation. The measured Hall resistivity shows anomalous Hall resistivity in its AIAO/AOAI antiferromagnetic phase. The observed anomalous Hall effect identifies the presence of WPs and the associated WSM phase in $\text{Sm}_2\text{Ir}_2\text{O}_7$ (111) thin films. We observed that the spin-structure-dependent magnetoresistance shows almost similar behavior, but the momentum space

Berry curvature $\Omega(\vec{k})$ induced anomalous or spontaneous Hall effect is very sensitive to the epitaxial strain.

II. EXPERIMENTAL DETAILS

Comprehensive temperature- and magnetic-field-dependent magnetotransport measurements have been performed on two $\text{Sm}_2\text{Ir}_2\text{O}_7$ (111) epitaxial thin films grown on (111)-oriented yttria-stabilized zirconia (YSZ) substrate. The two thin films having thicknesses of 65 nm and 50 nm are named S1 and S2, respectively. The epitaxial strain in the sample S2 is enhanced by growing on an atomically flat YSZ (111) substrate, made by air annealing at 1250 °C for 2 hours (details of the substrate preparation are discussed in the Supplemental Material [22]) [23], whereas sample S1 is deposited on an as-received YSZ (111) substrate with a comparatively rough surface (the atomic force microscopy scan of YSZ is shown in the Supplemental Material). The sample preparation procedure is similar to the previous report [24]. The crystallinity of the $\text{Sm}_2\text{Ir}_2\text{O}_7$ thin films was analyzed using a laboratory-based Rigaku SmartLab high-resolution four-circle x-ray diffractometer (XRD) ($\text{Cu-K}\alpha_1$ radiation). The oxidation states of the elements were characterized by x-ray photoelectron spectroscopy (XPS) using a Kratos Axis Ultra DLD system equipped with a monochromatic Al source ($K\alpha = 1486.6$ eV). We have kept pass energy at 20 eV and a step size of 0.1 eV during the measurement. Magnetization measurements of the films were done in a superconducting quantum interference device (SQUID) magnetometer (MPMS3, Quantum Design). The electrical and magnetotransport properties were measured in a physical property measurement system (PPMS, Quantum Design, with the electrical transport option) on a lithographically patterned Hall bar structure fabricated by physical Ar ion etching. Ohmic contacts were made by depositing Cr/Au (10/70 nm) contact pads in an e-beam evaporator. Finally, electrical connections have been made using ultrasonic wire bonding of Al wire (25 μm diameter) on the Cr/Au contact pads.

III. EXPERIMENTAL RESULTS

A. Structural analysis of $\text{Sm}_2\text{Ir}_2\text{O}_7$ (111) thin films

To identify the pyrochlore phase formation an XRD θ - 2θ scan is done on the postannealed $\text{Sm}_2\text{Ir}_2\text{O}_7$ thin film deposited on the (111)-oriented YSZ substrate and plotted in Fig. 2(a). It is observed that only (111)-oriented peaks of $\text{Sm}_2\text{Ir}_2\text{O}_7$ appear, which conforms to (111) directional growth of $\text{Sm}_2\text{Ir}_2\text{O}_7$. The appearance of odd-numbered peaks is a good confirmation of the pyrochlore phase of space group $Fd\bar{3}m$, which is a superstructure of fluorite structure ($Fm\bar{3}m$) consisting of only even-numbered peaks. To estimate the sample mosaic spread, a rocking curve measurement is performed around the $\text{Sm}_2\text{Ir}_2\text{O}_7$ (222) peak and plotted in Fig. 2(b); pseudo-Voigt fitting yields an FWHM value as low as 0.12°, which confirms good sample quality. The fully epitaxial growth of $\text{Sm}_2\text{Ir}_2\text{O}_7$ on YSZ is established from the appearance of the peaks in the same ϕ value for YSZ (331) and $\text{Sm}_2\text{Ir}_2\text{O}_7$ (662) planes in their azimuthal scans [as shown in Fig. 2(c)]. It implies a cube-on-cube epitaxial growth of

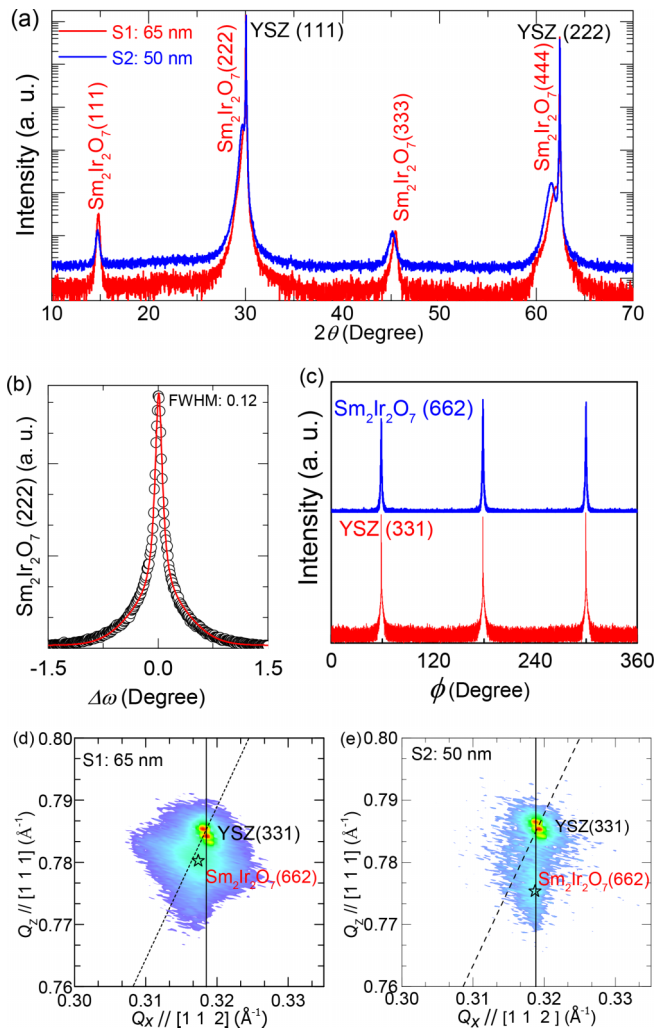


FIG. 2. (a) XRD θ - 2θ pattern of two postannealed $\text{Sm}_2\text{Ir}_2\text{O}_7$ (111) thin films named sample S1 (red) and sample S2 (blue), respectively. (b) Rocking curve measurement (ω scan) around $\text{Sm}_2\text{Ir}_2\text{O}_7$ (222) peak. (c) Azimuthal ϕ scan around $\text{Sm}_2\text{Ir}_2\text{O}_7$ (662) (blue line) and YSZ (331) (red line) peak. (d) and (e) are the asymmetric reciprocal space mapping around $\text{Sm}_2\text{Ir}_2\text{O}_7$ (662) and YSZ (331) peaks for the samples S1 and S2 having thicknesses of 65 nm and 50 nm, respectively. The vertical solid line represents coherent strained growth, whereas the dashed line passing through the origin of the Q_x - Q_z plot guides the relaxed cubic growth of $\text{Sm}_2\text{Ir}_2\text{O}_7$ on YSZ. The position of the $\text{Sm}_2\text{Ir}_2\text{O}_7$ (662) peak is identified with the black open star.

$\text{Sm}_2\text{Ir}_2\text{O}_7$ with the following epitaxial relation: (222)[222] $\text{Sm}_2\text{Ir}_2\text{O}_7$ \parallel (111)[111] YSZ and (224)[224] $\text{Sm}_2\text{Ir}_2\text{O}_7$ \parallel (112)[112] YSZ. The presence of three equally spaced peaks in the azimuthal scan confirms threefold cubic symmetry in the YSZ and $\text{Sm}_2\text{Ir}_2\text{O}_7$, respectively. In order to get information about the relaxed or strained growth of $\text{Sm}_2\text{Ir}_2\text{O}_7$ on YSZ, an asymmetric reciprocal space mapping (RSM) for all three samples around the YSZ (331) and $\text{Sm}_2\text{Ir}_2\text{O}_7$ (662) plane has been performed and plotted in the Q_x - Q_z plane. Figures 2(d) and 2(e) are the RSM plot of the samples S1 and S2, respectively. The vertical solid line parallel to the Q_z axis is a guideline for strained growth. The dashed line passing through

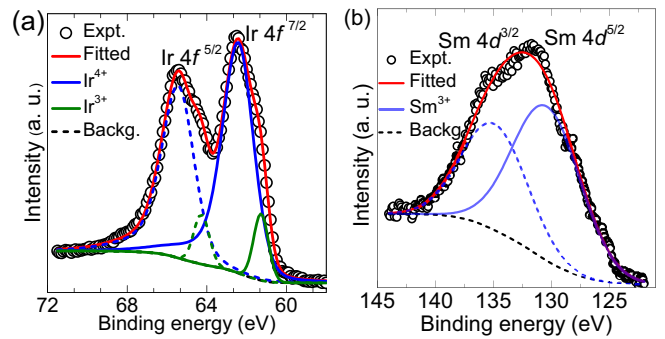


FIG. 3. Core level XPS spectra of sample S1. (a) Ir $4f^{5/2}$ and $4f^{7/2}$; each peak is fitted by considering two components and represented by a red line: higher (blue line) and lower (green line) binding energy components correspond to Ir^{4+} and Ir^{3+} , respectively. (b) Sm $4d^{3/2}$ and $4d^{5/2}$; each peak is fitted by considering a single component for Sm^{3+} and shown by the red line.

the origin of the Q_x - Q_z plot guides the relaxed cubic growth of $\text{Sm}_2\text{Ir}_2\text{O}_7$ on YSZ. The position of the $\text{Sm}_2\text{Ir}_2\text{O}_7$ (662) peak is marked by an open black star. The RSM plot of sample S1 shows that the $\text{Sm}_2\text{Ir}_2\text{O}_7$ (662) peak lies along the dashed line passing through the origin of the Q_x - Q_z plot. Therefore, it suggests the growth of sample S1 is mostly relaxed cubic growth, but due to the finite lattice mismatch between substrate and $\text{Sm}_2\text{Ir}_2\text{O}_7$, strain at the substrate and sample interface cannot be completely ruled out. The RSM plot of sample S2 shows that the $\text{Sm}_2\text{Ir}_2\text{O}_7$ (662) peak lies along the vertical line but is well separated from the YSZ (331) peak, suggesting that the in-plane lattice parameter of $\text{Sm}_2\text{Ir}_2\text{O}_7$ is completely locked to the YSZ, which is expected as this particular sample is grown on an atomically flat YSZ (111) substrate. Due to the finite lattice mismatch between $\text{Sm}_2\text{Ir}_2\text{O}_7$ and YSZ, the out-of-plane lattice parameter of $\text{Sm}_2\text{Ir}_2\text{O}_7$ will be modified (here it is expanded) to accommodate the unit cell volume. Therefore, the RSM analysis of the two samples suggests the strength of in-plane compressive strain is maximum for sample S2.

B. X-ray photoelectron spectroscopy

It is realized that the electrical transport and magnetic properties of pyrochlore iridates ($\text{A}_2\text{Ir}_2\text{O}_7$) significantly depend on the oxidation states of the individual cation [9,25]. The oxidation states of the cations of the postannealed $\text{Sm}_2\text{Ir}_2\text{O}_7$ films were studied by XPS measurements. All the measured XPS spectra were calibrated using the C 1s peak by fixing the binding energy at 284.8 eV. Deconvolution of the spectrum was performed using the Gaussian-Lorentz (GL) peak profile function in standard XPSPEAK4.1 software. The Shirley background function has been used for the background correction. The spin-orbit split spectra of the Ir $4f$ core level are plotted in Fig. 3(a). Both Ir $4f^{7/2}$ and $4f^{5/2}$ peaks were fitted using a two-peak function, where the lower binding energy corresponds to Ir^{3+} , and the higher binding energy corresponds to Ir^{4+} oxidation states. The binding energies from the fitting for the two $4f^{7/2}$ ($4f^{5/2}$) peaks are found to be 62.4 eV (65.4 eV) and 61.2 eV (64.2 eV), respectively. The spin-orbit splitting between Ir $4f^{5/2}$ and $4f^{7/2}$ appeared

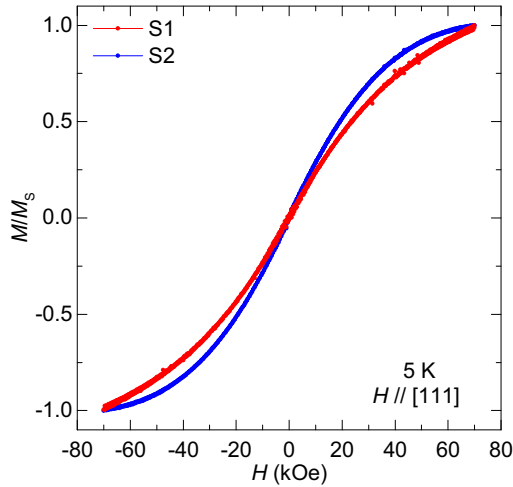


FIG. 4. Magnetic field dependence of normalized magnetization (M/M_s) of $\text{Sm}_2\text{Ir}_2\text{O}_7$ (111) thin film at 5 K, for the applied field along [111] direction; red and blue curves denote the magnetization data for samples S1 and S2, respectively.

to be 3 eV, which is in good agreement with the reported value [26]. The estimated relative ratio of $\text{Ir}^{4+} : \text{Ir}^{3+}$ comes to be 0.903 : 0.096. The observed mixed oxidation states of Ir are likely due to oxygen deficiency in the sample [25,27,28]. Figure 3(b) shows spin-orbit split spectra of the Sm 4d core level. The binding energy of the $4d^{5/2}$ and $4d^{3/2}$ peaks was found to be 130.3 eV and 134.9 eV, respectively, which we assign for Sm^{3+} . The spin-orbit splitting between Sm $4d^{5/2}$ and $4d^{3/2}$ appeared to be 4.6 eV, which is very close to the earlier reported value of 4.9 eV [29]. Our XPS analysis suggests that the Ir oxidation states are more sensitive to oxygen deficiency than Sm.

C. Magnetometry measurements of samples S1 and S2

Figure 4 shows the magnetic-field-dependent normalized magnetization (M/M_s) of $\text{Sm}_2\text{Ir}_2\text{O}_7$ (111) thin films at 5 K for an applied field along the [111] direction. The red and blue curves denote the magnetization data for samples S1 and S2, respectively. The magnetization shows a nonlinear variation with the applied H , without any hysteresis between the field sweep-up and sweep-down process. This nonhysteretic behavior appears as the Ir^{4+} sublattices order in a compensated AIAO/AOAI noncollinear antiferromagnetic spin structure, which causes field-induced magnetization, whereas the Sm^{3+} moments remain in the paramagnetic phase.

D. Longitudinal resistivity of sample S1

Electrical transport, the variation of the resistivity of a material, is usually a crucial step in identifying novel functionalities. For the presence of competing energy scales like electron correlation and spin-orbit coupling, materials often exhibit a metal-insulator (semimetal) transition, which behaves as a hallmark of many functional quantum materials [30]. Here, the temperature variation of longitudinal resistivity [$\rho_{xx}(T)$] along with its temperature derivative ($d\rho_{xx}/dT$) for the $\text{Sm}_2\text{Ir}_2\text{O}_7$ (111) thin film is plotted in Fig. 5(a); the

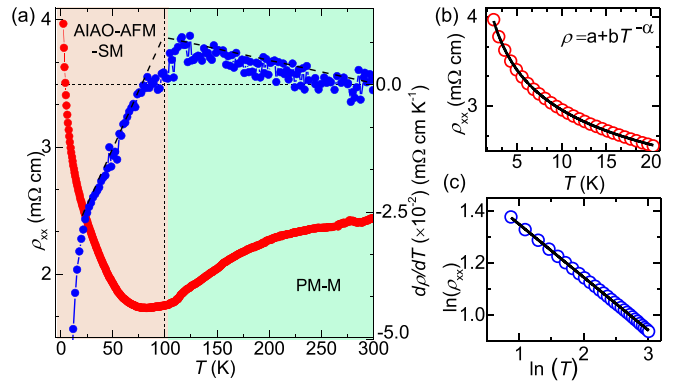


FIG. 5. (a) Temperature dependence of longitudinal resistivity (ρ_{xx}) (solid red circle) and corresponding temperature derivative plot (solid blue circle) of $\text{Sm}_2\text{Ir}_2\text{O}_7$ (111) thin film, showing a metal-semimetal transition around 100 K. Red and green regions indicate paramagnetic metallic (PM-M) and all-in-all-out antiferromagnetic semimetallic (AIAO-AFM-SM) phases, respectively. The low-temperature (2–20 K) resistivity data follow a gapless semimetallic behavior, where (b) is the power-law $\rho = a + bT^{-\alpha}$ fitting, denoted by the black curve. (c) $\ln(\rho)$ versus $\ln(T)$ plot in the temperature range of 2–20 K; black curve represents a straight-line fitting with a slope of $-\alpha$.

solid red and blue circles represent them, respectively. As the sample is cooled down from 300 K, the value of ρ_{xx} decreases continuously down to 100 K and has broad minima around 100 K, below which resistivity increases with a decrease in temperature down to the lowest measured temperature 2 K. The apparent change in resistivity behavior around 100 K is associated with the all-in-all-out/all-out-all-in (AIAO/AOAI) magnetic ordering of Ir^{4+} 5d moments from its paramagnetic metallic phase [7]. The transition point (T_{MI}) is more clearly identified by the intersection of two straight lines (black dashed line) extrapolated by fitting the high- and low-temperature part of the derivative curve, and it appears at 100 K. Though in $\text{Sm}_2\text{Ir}_2\text{O}_7$ Sm^{3+} has nonzero 4f moments, no signature of its magnetic ordering is reflected in the resistivity data down to the lowest measured temperature of 2 K. Earlier temperature-dependent x-ray diffraction study on the similar compound $\text{Eu}_2\text{Ir}_2\text{O}_7$ could not detect any change in lattice structure below the transition temperature [31]. However, a recent synchrotron study on $\text{Eu}_2\text{Ir}_2\text{O}_7$ by Das *et al.* revealed a finite nonmonotonic change in the microscopic parameters of IrO_6 octahedra (Ir-O1 bond length, Ir-O1-Ir and O1-Ir-O1 bond angle) across the metal-semimetal transition [32]. The temperature-dependent Raman spectroscopy study by Udea *et al.* on $\text{Eu}_2\text{Ir}_2\text{O}_7$ has also observed some anomalies in the phonon mode associated with an Ir-O-Ir bond bending across the metal-semimetal transition [33]. This indicates the presence of finite electron-lattice interaction, which may be a possible underlying mechanism of the observed metal-semimetal transition.

A close look at the high-temperature (above 100 K) metallic phase shows the rate of resistivity changes decreases with an increase in temperature, which is more evident in the derivative plot; as the temperature increases the value of $d\rho_{xx}/dT$ decreases and becomes almost zero at 300 K.

This resistivity saturation is also observed in other pyrochlore iridates [34,35]. For materials that exhibit a metal-insulator (semimetal) transition, properties of the metallic phase are generally quite different from the ordinary metals, as observed by transport, magnetic, and optical studies [30]. The unusual properties of the metallic phase above the transition have been studied mostly for d -electron systems. Earlier theoretical calculations also predicted NFL behavior for the pyrochlore iridates in the presence of spin-orbit coupling [36,37].

The low-temperature (2–20 K) resistivity data, which follow a power law of temperature dependence ($\rho \sim a + bT^{-\alpha}$), are shown in Fig. 5(b) (the black line represent the power-law fitting). The power-law dependence is more clear in the $\ln(\rho_{xx})$ versus $\ln(T)$ plot in Fig. 5(c), which follows a straight line with a slope of $\alpha = 0.2$. The temperature dependence of longitudinal resistivity, along with its temperature derivative and power-law fitting (with $\alpha \sim 1.3$) for the sample S2, is shown in the Supplemental Material [22]. The variation in the α values might arise due to slight changes in the structural parameter and their respective electronic band structure. However, the effect of the crystalline disorder cannot be completely ruled out. This power-law dependence of resistivity corresponds to a gapless semimetallic charge transport [14,24].

E. Magnetoresistance of sample S1

The itinerant electrons on geometrically frustrated lattices offer new opportunities for studying their magnetic-field-induced modified magnetic/spin structure and associated electronic transport properties. Here, we have studied the possible field-induced modification of the spin structure by means of magnetoresistance (MR) measurements (data for sample S1 are shown here, whereas data for sample S2 are shown in the Supplemental Material [22]). In order to check the sample reproducibility, MR measurements were also performed on another sample S3 (~ 65 nm thick), the structural, longitudinal resistivity, and MR data of which are shown in the Supplemental Material. Figure 6(a) shows the low-temperature (2–5 K) MR data of $\text{Sm}_2\text{Ir}_2\text{O}_7$ (111) thin film for the applied field along the [111] direction. It shows negative MR up to the highest measured field of 100 kOe without any sign of saturation or any kind of hysteresis. With a close look, it can be seen that in the low-field regime (below 50 kOe), the MR data vary almost quadratically and above, which changes more likely as linear. The change in MR behavior is more visible in the corresponding field-derivative (dMR/dH) plot, as shown in Fig. 6(b). Below 50 kOe, the dMR/dH varies close to linear and above, which shows a tendency of saturation. The absence of hysteresis and small nonsaturating negative MR (in the temperature range of 2–5 K) occurs mostly due to the reversible spin canting of the Ir^{4+} 5d moments along the applied field (H) direction.

MR data for the temperature range of 10–20 K are plotted in Fig. 6(c) (MR data for the other temperatures are shown in the Supplemental Material [22]). It is seen that in the 10 K onward MR data, finite hysteresis is present, which disappears above 100 K (the AIAO/AOAI AFM ordering temperature). Hysteretic MR is also observed in other pyrochlore iridates having magnetic ($\text{Nd}_2\text{Ir}_2\text{O}_7$, $\text{Tb}_2\text{Ir}_2\text{O}_7$)

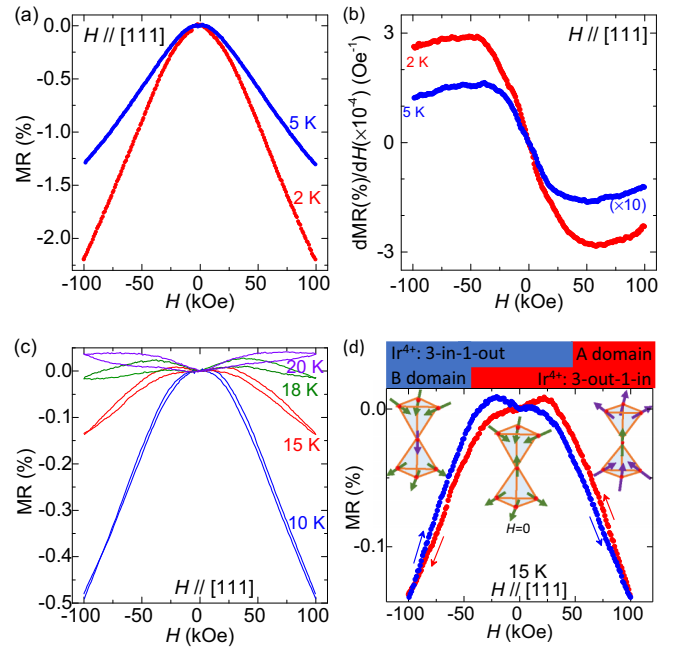


FIG. 6. Magnetic field dependence of nonhysteretic low-temperature (2–5 K) (a) magnetoresistance (MR) and (b) corresponding first-derivative plot (5 K data have been scaled up) for the applied field along [111] direction. Hysteretic MR plot (c) for the intermediate temperature regime (10–20 K). (d) MR plot at 19 K, the possible spin structure and domain configuration of Ir^{4+} 5d moments, for the applied field along [111] direction is shown by schematics, where 3-out-1-in and 3-in-1-out terminologies represent the spin configuration of upper tetrahedrons of the corner-sharing tetrahedral network.

[11–13,38,39] as well as nonmagnetic ($\text{Eu}_2\text{Ir}_2\text{O}_7$) [14,15,40] rare earth cations (RE^{3+}). In addition to the hysteresis, for 10–18 K MR data, in the low-field regime, it shows positive MR, and in the intermediate field, it crosses over and remains negative up to the maximum measured field of 100 kOe, whereas for 20–100 K MR is completely positive up to the highest measured field of 100 kOe. To see the positive to negative crossover and explain the hysteretic MR phenomena, we have separately plotted 19 K MR data in Fig. 6(d). For pyrochlore iridates in the AFM-ordered ground ($H = 0$) state, as both the AIAO (A-domain) and AOAI (B-domain) spin configuration have the same energy, both will be stabilizing in equal proportion in the sample. The typical size of the domain is 1–2 μm [39], which is very small compared to the size of the Hall bar ($190 \times 100 \mu\text{m}^2$) used in our experiments. Previous reports showed that the field-cooling domain imbalance could cause asymmetric MR responses, which will reverse sign by reversing the cooling field direction [24,41]. Therefore, the appearance of hysteresis above 10 K onward can be attributed to the field-induced plastic domain deformation in association with a change in the spin structure from AIAO (4-in-0-out) to 3-out-1-in, as observed in other pyrochlore iridates also [11–15,40].

In an applied magnetic field, competition or cooperation between different magnetic interactions can cause various spin configurations. In this present case, the field-induced

modification of the Ir^{4+} spin structure can be understood from the classical Ising Hamiltonian (\mathcal{H}) in an applied magnetic field:

$$\mathcal{H} = -\frac{1}{2}J \sum_{i,j} \mathbf{S}_i^{z_i} \cdot \mathbf{S}_j^{z_j} - \sum_i \mathbf{H} \cdot \mathbf{S}_i^{z_i};$$

for the first AFM exchange interaction term summation is over the nearest neighbors, whereas the second term accounts for the field-induced Zeeman energy at finite H ; $\mathbf{S}_i^{z_i}$ is the moment on the i th site with its own local Ising axis \mathbf{z}_i directed along the $\langle 111 \rangle$ direction, constrained to be either toward or away from the center of the tetrahedron. In an applied magnetic field along the $[111]$ direction, the spin structure can change from 4-in-0-out to 3-out-1-in such that the total energy gets minimized. Field-induced modification of the Ir^{4+} $5d$ moment spin structures are shown by schematics in Fig. 6(d). Nonhysteretic MR below 10 K suggests that below 10 K, the AFM interaction between Ir^{4+} $5d$ moments is strong enough against the applied magnetic field (at least 100 kOe), and no field-induced plastic domain switching occurs, whereas hysteretic MR suggests that above 10 K onward, AFM interaction is weak enough against the applied magnetic field and causes a field-induced change in the spin structure.

It is seen that the positive to negative crossover and hysteresis in MR start appearing from the same temperature (10 K onward). Therefore, the crossover in MR is also most likely to occur due to the change in the spin structure of Ir^{4+} $5d$ moments. In addition, it is observed that the hysteretic MR does not close throughout the measured field, even up to the highest measured field of 100 kOe. Earlier studies on the similar compound $\text{Eu}_2\text{Ir}_2\text{O}_7$ also observed nonclosing hysteretic MR behavior [14,15,40]. This nonclosing MR phenomenon suggests that even 100 kOe of an applied magnetic field is not sufficient enough for complete domain switching. This detailed MR study suggests that any field-induced modification of the spin structure and plastic domain deformation is reflected in the observed MR behavior. These changes in electrical resistance due to modification of the spin structure suggest a strong coupling between the spin and charge degrees of freedom in $\text{Sm}_2\text{Ir}_2\text{O}_7$.

F. Anomalous and spontaneous Hall resistivity

Identifying the quantum state in quantum material provides the most direct manifestation of the underlying abstract physics. ‘‘Quantum’’ means the quantum phase (Berry phase) of the electronic wave function. Of particular interest is a manipulation of the Berry curvature. One efficient way to get information about the momentum space Berry curvature is by measuring the intrinsic anomalous Hall conductivity (AHC) [42]. For studying how the epitaxial-strain-induced modification (if any) of the electronic band structure and associated Berry curvature influence electronic transport properties, we have performed Hall measurements on $\text{Sm}_2\text{Ir}_2\text{O}_7$ (111) thin films having relaxed (sample S1) as well strained (sample S2) growth.

The magnetic field dependence of Hall resistivity (ρ_{xy}) at various temperatures of the sample S1 (mostly relaxed growth) for an applied field along the $[111]$ direction is

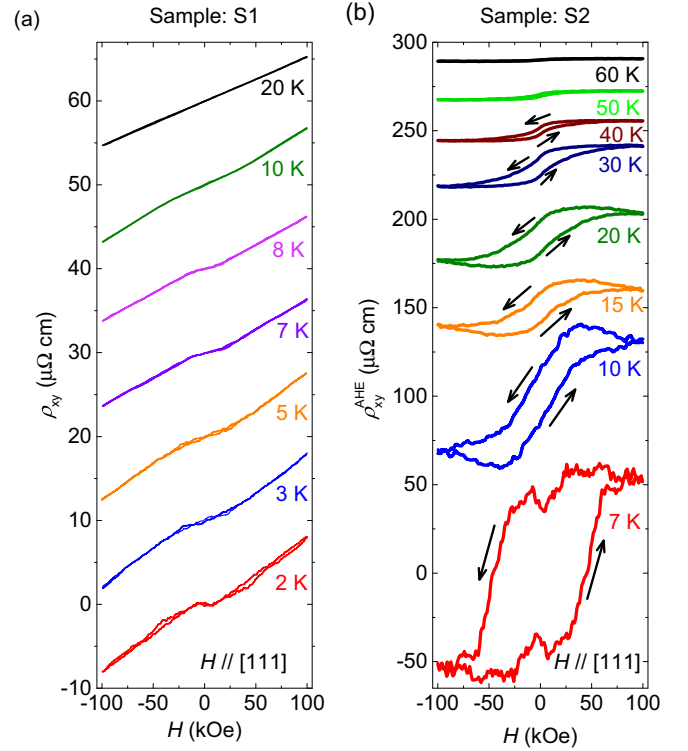


FIG. 7. Magnetic field dependence of (a) measured Hall resistivity (ρ_{xy}) of the sample S1 and (b) anomalous Hall resistivity (ρ_{xy}^{AHE}) (after subtracting the ordinary Hall component) of the sample S2, at different temperatures, for the applied field along $[111]$ direction. For better visual clarity, the data [except 2 K data in panel (a) and 7 K data in panel (b)] are shifted vertically.

plotted in Fig. 7(a). It is seen that for the 2 K data (red curve) in the low-field regime, the Hall resistivity varies nonmonotonically, whereas in the high-field regime it is linear. The low-field nonlinearity decreases as the temperature increases and vanishes above 10 K. This nonlinear component is also observed in other pyrochlore iridates, called the anomalous Hall effect (AHE), which arises mainly due to the momentum space Berry curvature $[\Omega(\vec{k})]$ [14,17]. The anomalous Hall resistivity (ρ_{xy}^{AHE}) (after subtracting the ordinary Hall component) for the sample S2 (coherent strained growth) at various temperatures for the applied field along the $[111]$ direction is shown in Fig. 7(b) (where the field sweep process is marked by black arrows). In addition to the nonlinearity finite hysteresis is observed between the field sweep-up and sweep-down processes, whereas the magnetization data do not show any hysteresis [$M(H=0) \approx 0$] as shown in Fig. 4. By a close examination of Figs. 7(a) and 7(b) it can be seen that the anomalous components (nonlinear components) have the opposite sign to each other. To clearly see the sign change of the AHE, in the Supplemental Material [22] we have plotted only the 7 K anomalous Hall component (after subtracting the ordinary Hall contribution) for samples S1 and S2. The intrinsic anomalous Hall conductivity (AHC) is determined by integrating the $\Omega(\vec{k})$ of the filled bands over the whole

BZ [42,43]:

$$\sigma_{xy}^{\text{AHC}} = \frac{e^2}{\hbar} \int_{\text{BZ}} \frac{d^3\vec{k}}{(2\pi)^3} \sum_n f(\epsilon_n(\vec{k}) - \mu) \Omega_{xy}(\vec{k}),$$

where μ is the chemical potential and $f(\epsilon_n(\vec{k}) - \mu)$ is the Fermi-Dirac distribution function. Therefore, one can expect that the finite epitaxial strain and (Ir/Sm) off-stoichiometry in the sample S2 modify the electronic band dispersion and band filling in such a way that the combined effect of Berry curvature [$\Omega(\vec{k})$] and the position of the Fermi level (E_F) give rise to changes in the sign of the AHE. In a perfect cubic lattice, due to the presence of twofold rotational symmetries C_2 about the x , y , and z axis $\Omega(\vec{k})$ will be canceled by $\Omega(C_2(\vec{k}))$; as a result the net contribution of $\Omega(\vec{k})$ to the AHE will be hidden. Therefore, the C_2 symmetry needs to be broken to observe an AHE; in this study, the strained growth of sample S2 will help to break the C_2 symmetry. Earlier theoretical calculations for pyrochlore iridates (in the WSM phase) for an applied pressure along the [111] direction or in the (111)-oriented thin film geometry predicted that the AHC (σ_{xy}^{AHC}) is directly proportional to the separation between the WPs [3,21]. For the presence of only a pair of WPs in the BZ, $\sigma_{xy}^{\text{AHC}} = (e^2/h)(2k_0/2\pi)$, where $2k_0$ is the separation between two WPs inside the BZ [21,44]. In the extreme case, when the WPs are moved to the BZ boundary, and two WPs with opposite chirality meet and are annihilated, the system can become a quantized 3D anomalous Hall state. Therefore, in addition to the change in the sign of the AHE, the observation of a large spontaneous Hall effect (SHE) in sample S2 suggests the position of the WPs might be quite different with respect to sample S1. Earlier theoretical and experimental studies on $\text{Nd}_2\text{Ir}_2\text{O}_7$ (111) thin films showed that even $\sim 1\%$ compressive stain significantly modifies the band dispersion and the Berry curvature, which leads to finite SHE [16]. For $\text{Pr}_2\text{Ir}_2\text{O}_7$ (111) thin films finite epitaxial strain stabilizes bulk absent AIAO magnetic order, and the corresponding WSM phase exhibits finite SHE [17,45,46].

Takahashi *et al.* have shown that in a multiband magnetic semiconductor La-doped EuTiO_3 , electron doping can control the Berry curvature and results in a sign reversal in the observed AHE [47]. Epitaxial-strain-induced

manipulation of Berry curvature and change in sign and amplitude of the anomalous Hall effect is also observed by Tian *et al.* for SrRuO_3 thin films [48]. Recent theoretical calculation on the antiperovskite Mn_3NiN has predicted a large increment of the AHC by controlling the Berry curvature through an epitaxial strain [49]. Therefore, this strain-induced change in sign of AHE and observation of large intrinsic spontaneous Hall effect ($\sim 50 \mu\Omega \text{ cm}$, at 7 K) signifies the presence of WPs and conforms the WSM phase of $\text{Sm}_2\text{Ir}_2\text{O}_7$ in its thin film geometry.

IV. CONCLUSION

In conclusion, a metal-semimetal transition concomitant with an all-in-all-out (AIAO) magnetic order of Ir^{4+} is observed in the $\text{Sm}_2\text{Ir}_2\text{O}_7$ (111) thin films. The magnetotransport studies revealed that in the low-temperature (\sim below 10 K), the AIAO spin structure is robust against the applied magnetic field, but 10 K onward field-induced modification of the spin structure and domain imbalance occurs. We observed that an epitaxial strain in $\text{Sm}_2\text{Ir}_2\text{O}_7$ (111) thin films causes a sign change in the anomalous Hall effect and induces a large spontaneous Hall effect (SHE) ($\sim 50 \mu\Omega \text{ cm}$, at 7 K) present up to elevated temperatures (60 K). The observation of large SHE without notable magnetization identifies the fingerprint of Weyl points and confirms the theoretically predicted Weyl semimetallic phase in $\text{Sm}_2\text{Ir}_2\text{O}_7$. We attribute this enhancement of SHE to the possible modification of the electronic band structure close to the Fermi level (E_F) and the associated Berry curvature [$\Omega(\vec{k})$]. Therefore, our findings reveal a distinct correlation between the SHE and the Berry curvature ($\Omega_{[111]}(\vec{k})$) as a function of epitaxial strain. The Berry curvature and the epitaxial strain act as the source and control mechanism of this anomalous transport phenomenon. This strain-engineering approach can be further extended to hunt for new topological properties in other correlated magnetic materials, which will deepen the understanding of the underlying fundamental mechanisms.

ACKNOWLEDGMENTS

M.G. would like to thank MHRD, India, for financial support. P.S.A.K. acknowledges Nano Mission, DST, India, for funding support.

-
- [1] D. Pesin and L. Balents, *Nat. Phys.* **6**, 376 (2010).
 - [2] X. Wan, A. M. Turner, A. Vishwanath, and S. Y. Savrasov, *Phys. Rev. B* **83**, 205101 (2011).
 - [3] K. Y. Yang, Y. M. Lu, and Y. Ran, *Phys. Rev. B* **84**, 075129 (2011).
 - [4] W. Witczak-Krempa and Y. B. Kim, *Phys. Rev. B* **85**, 045124 (2012).
 - [5] W. Witczak-Krempa, G. Chen, Y. B. Kim, and L. Balents, *Annu. Rev. Condens. Matter Phys.* **5**, 57 (2014).
 - [6] D. Yanagishima and Y. Maeno, *J. Phys. Soc. Jpn.* **70**, 2880 (2001).
 - [7] K. Matsuhira, M. Wakeshima, R. Nakanishi, T. Yamada, A. Nakamura, W. Kawano, S. Takagi, and Y. Hinatsu, *J. Phys. Soc. Jpn.* **76**, 043706 (2007).
 - [8] K. Matsuhira, M. Wakeshima, Y. Hinatsu, and S. Takagi, *J. Phys. Soc. Jpn.* **80**, 094701 (2011).
 - [9] A. Banerjee, J. Sannigrahi, S. Giri, and S. Majumdar, *Phys. Rev. B* **96**, 224426 (2017).
 - [10] K. Matsuhira, M. Tokunaga, M. Wakeshima, Y. Hinatsu, and S. Takagi, *J. Phys. Soc. Jpn.* **82**, 023706 (2013).
 - [11] K. Ueda, J. Fujioka, B. J. Yang, J. Shiozaki, A. Tsukazaki, S. Nakamura, S. Awaji, N. Nagaosa, and Y. Tokura, *Phys. Rev. Lett.* **115**, 056402 (2015).

- [12] Z. Tian, Y. Kohama, T. Tomita, H. Ishizuka, T. Hsieh, J. J. Ishikawa, K. Kindo, L. Balents, and S. Nakatsuji, *Nat. Phys.* **12**, 134 (2016).
- [13] W. J. Kim, J. H. Gruenewald, T. Oh, S. Cheon, B. Kim, O. B. Korneta, H. Cho, D. Lee, Y. Kim, M. Kim *et al.*, *Phys. Rev. B* **98**, 125103 (2018).
- [14] M. Ghosh, D. Samal, and P. S. Anil Kumar, *Phys. Rev. B* **106**, 085139 (2022).
- [15] X. Liu, S. Fang, Y. Fu, W. Ge, M. Kareev, J. W. Kim, Y. Choi, E. Karapetrova, Q. Zhang, L. Gu *et al.*, *Phys. Rev. Lett.* **127**, 277204 (2021).
- [16] W. J. Kim, T. Oh, J. Song, E. K. Ko, Y. Li, J. Mun, B. Kim, J. Son, Z. Yang, Y. Kohama *et al.*, *Sci. Adv.* **6**, eabb1539 (2020).
- [17] Y. Li, T. Oh, J. Son, J. Song, M. K. Kim, D. Song, S. Kim, S. H. Chang, C. Kim, B. J. Yang *et al.*, *Adv. Mater.* **33**, 2008528 (2021).
- [18] T. Kondo, M. Nakayama, R. Chen, J. J. Ishikawa, E. G. Moon, T. Yamamoto, Y. Ota, W. Malaeb, H. Kanai, Y. Nakashima *et al.*, *Nat. Commun.* **6**, 10042 (2015).
- [19] C. Donnerer, M. C. Rahn, M. M. Sala, J. G. Vale, D. Pincini, J. Strempler, M. Krisch, D. Prabhakaran, A. T. Boothroyd, and D. F. McMorrow, *Phys. Rev. Lett.* **117**, 037201 (2016).
- [20] R. Asih, N. Adam, S. S. Mohd-Tajudin, D. P. Sari, K. Matsuhira, H. Guo, M. Wakeshima, Y. Hinatsu, T. Nakano, Y. Nozue *et al.*, *J. Phys. Soc. Jpn.* **86**, 024705 (2017).
- [21] B. J. Yang and N. Nagaosa, *Phys. Rev. Lett.* **112**, 246402 (2014).
- [22] See Supplemental Material at <http://link.aps.org/supplemental/10.1103/PhysRevB.108.075145> for atomic force microscopy images of the YSZ (111) substrate, higher temperature magnetoresistance data for sample S1, structural and electrical transport data for sample S2, 7 K anomalous Hall resistivity data for sample S1 and S2, structural and electrical transport data for sample S3.
- [23] T. Honke, H. Fujioka, J. Ohta, and M. Oshima, *J. Vac. Sci. Technol. A* **22**, 2487 (2004).
- [24] M. Ghosh, S. G. Bhat, A. Pal, and P. S. A. Kumar, *J. Phys.: Condens. Matter* **34**, 165701 (2022).
- [25] W. C. Yang, W. K. Zhu, H. D. Zhou, L. Ling, E. S. Choi, M. Lee, Y. Losovyj, C. K. Lu, and S. X. Zhang, *Phys. Rev. B* **96**, 094437 (2017).
- [26] G. K. Wertheim and H. J. Guggenheim, *Phys. Rev. B* **22**, 4680 (1980).
- [27] W. C. Yang, Y. Y. Xie, W. K. Zhu, Y. Park, A. P. Chen, Y. Losovyj, Z. Li, H. M. Liu, M. Starr, A. J. Acosta *et al.*, *Sci. Rep.* **7**, 7740 (2017).
- [28] Y. Wu, M. Li, X. Li, and J. Xie, *J. Low Temp. Phys.* **202**, 48 (2021).
- [29] Y. Uwamino, T. Ishizuka, and H. Yamatera, *J. Electron Spectrosc. Relat. Phenom.* **34**, 67 (1984).
- [30] M. Imada, A. Fujimori, and Y. Tokura, *Rev. Mod. Phys.* **70**, 1039 (1998).
- [31] H. Takatsu, K. Watanabe, K. Goto, and H. Kadowaki, *Phys. Rev. B* **90**, 235110 (2014).
- [32] M. Das, S. Bhowal, J. Sannigrahi, A. Bandyopadhyay, A. Banerjee, G. Cibin, D. Khalyavin, N. Banerjee, D. Adroja, I. Dasgupta *et al.*, *Phys. Rev. B* **105**, 134421 (2022).
- [33] K. Ueda, R. Kaneko, A. Subedi, M. Minola, B. J. Kim, J. Fujioka, Y. Tokura, and B. Keimer, *Phys. Rev. B* **100**, 115157 (2019).
- [34] F. F. Tafti, J. J. Ishikawa, A. McCollam, S. Nakatsuji, and S. R. Julian, *Phys. Rev. B* **85**, 205104 (2012).
- [35] P. Telang, K. Mishra, A. K. Sood, and S. Singh, *Phys. Rev. B* **97**, 235118 (2018).
- [36] E. G. Moon, C. Xu, Y. B. Kim, and L. Balents, *Phys. Rev. Lett.* **111**, 206401 (2013).
- [37] H. Shinaoka, S. Hoshino, M. Troyer, and P. Werner, *Phys. Rev. Lett.* **115**, 156401 (2015).
- [38] T. C. Fujita, Y. Kozuka, J. Matsuno, M. Uchida, A. Tsukazaki, T. Arima, and M. Kawasaki, *Phys. Rev. Mater.* **2**, 011402(R) (2018).
- [39] T. C. Fujita, M. Uchida, Y. Kozuka, W. Sano, A. Tsukazaki, T. Arima, and M. Kawasaki, *Phys. Rev. B* **93**, 064419 (2016).
- [40] L. Xu, G. Gong, C. Zhao, X. Song, S. Yuan, and Z. Tian, *J. Phys. Chem. C* **124**, 22656 (2020).
- [41] T. C. Fujita, Y. Kozuka, M. Uchida, A. Tsukazaki, T. Arima, and M. Kawasaki, *Sci. Rep.* **5**, 9711 (2015).
- [42] Z. Fang, N. Nagaosa, K. S. Takahashi, A. Asamitsu, R. Mathieu, T. Ogasawara, H. Yamada, M. Kawasaki, Y. Tokura, and K. Terakura, *Science* **302**, 92 (2003).
- [43] M. Onoda and N. Nagaosa, *J. Phys. Soc. Jpn.* **71**, 19 (2002).
- [44] A. A. Burkov and L. Balents, *Phys. Rev. Lett.* **107**, 127205 (2011).
- [45] L. Guo, N. Campbell, Y. Choi, J. W. Kim, P. J. Ryan, H. Huyan, L. Li, T. Nan, J. H. Kang, C. Sundahl *et al.*, *Phys. Rev. B* **101**, 104405 (2020).
- [46] T. Ohtsuki, Z. Tian, A. Endo, M. Halim, S. Katsumoto, Y. Kohama, K. Kindo, M. Lippmaa, and S. Nakatsuji, *Proc. Natl. Acad. Sci. USA* **116**, 8803 (2019).
- [47] K. S. Takahashi, H. Ishizuka, T. Murata, Q. Y. Wang, Y. Tokura, N. Nagaosa, and M. Kawasaki, *Sci. Adv.* **4**, eaar7880 (2018).
- [48] D. Tian, Z. Liu, S. Shen, Z. Li, Y. Zhou, H. Liu, H. Chen, and P. Yu, *Proc. Natl. Acad. Sci. USA* **118**, e2101946118 (2021).
- [49] A. Torres-Amaris, A. Bautista-Hernandez, R. Gonzalez-Hernandez, A. H. Romero, and A. C. Garcia-Castro, *Phys. Rev. B* **106**, 195113 (2022).